DESIGN AND FABRICATION OF INTEGRATED PARABOLIC REFLECTOR NANO-ANTENNA COUPLED INFRARED DETECTOR

MOHAMED HABASHY MUBARAK RAMADAN

UNIVERSITI SAINS MALAYSIA

2018

DESIGN AND FABRICATION OF INTEGRATED PARABOLIC REFLECTOR NANO-ANTENNA COUPLED INFRARED DETECTOR

by

MOHAMED HABASHY MUBARAK RAMADAN

Thesis submitted in fulfilment of
the requirements for the degree of
Doctor of Philosophy

April 2018

ACKNOWLEDGEMENTS

First of all, I would like to dedicate all praise to Allah for all of HIS support and apparent and non apparent bounties and favors during all my life and throughout my PhD programme as well.

I would like then to tender my gratitude to all my Professors since I started my programme, Professor Dato' Dr. Ahmad Shukri Mustapa Kamal, Professor Dr. Othman Sidek, Dr. Mohd Tafir Mustaffa, Dr. Mohamed A.Ramy, and my previous co-supervisor as well Dr. Magdy H. Mourad for their guidance, support, and encouragement during their supervision. May Allah, SWT, reward them for all their support in this present and the future life.

My deep appreciation goes also to Dr. Khairudin Mohamed for his continued support, useful discussion and consultation, and facilitation in the laboratory during my work.

I would also like here also to take this opportunity to express my appreciation to my School of Electrical Engineering, Universiti Sains Malaysia for facilitating my research requirement and providing me with an excellent academic environment that has helped me to complete this work successfully. Among all my colleagues in our school, my appreciation goes also to my colleague Yee Ming Chung especially for all his efforts and support. My Special regards also to the technical staff as well as my colleagues in both the Nano-Optoelectronics Research (NOR) laboratory and the Nano-fabrication and Functional Materials (NFM) laboratory for their useful technical discussion and assistance during the experimental work. Among all the staff members and colleagues, I dedicate a special recognition to Eng. Mohd Anas Ahmad, Enc.

Abdul Jamil Yusuf, NuraLiman Chiromawa, Siti Suhaila bnti Md Izah and Mohamed Kamarul Aizat, I wish them God's guidance in their future endeavors.

Finally, gratitude and thankfulness to my parents and my family for being patient during all these years of struggling in my way towards my PhD certificate.

TABLE OF CONTENTS

Page

ACKNOWLEDGEMENTS ii

TABLE OF CONTENTS iv

LIST OF TABLES ix

LIST OF FIGURES x

LIST OF ABBREVIATIONS xv

ABSTRAK xix

ABSTRACT xxi

CHAPTER ONE: INTRODUCTION

1.1 Infrared Detection 1

1.2 Nano-Antenna Coupled IR Detectors 3

1.3 Statement of the Problem 4

1.4 Research Objectives 6

1.5 Scope and Limitations 7

1.6 Thesis Outline 7

CHAPTER TWO: RESEARCH BACKGROUND

2.1 Introduction 9

2.2 Device Fabrication 13

- 2.2.1 Nano Lithography Techniques 14
  - 2.2.1(a) E-beam Resist and Liftoff Techniques 17
  - 2.2.1(b) Shadow Masking Technique 18

2.2.2 3D Micro-machining and Etching Techniques 19

2.3 Antenna Design 23

2.3.1 Dielectric Half-Space and Angular Response 24

2.3.2 Antenna Effective Resonant Length 27

2.3.3 Surface Waves 30

2.3.4 Antenna Current Distribution 32

2.3.5 Antenna Arrays and Effective Aperture 34

2.3.6 Parabolic Reflector Antenna 36

2.4 IR Sensing Element 38

2.4.1 Metal Oxide Metal (MOM) Diode 40

2.4.1(a) Transduction Mechanism and I-V Characteristics 41

2.4.1(b) Diode Resistance 43

2.4.1(c) Cut-off Frequency 44

2.4.1(d) Breakdown Voltage 45

2.4.2 Bolometer 46

2.5 Impedance Matching Consideration 49

2.6 Fabricated Device Characterization 51

2.6.1 Morphology Analysis 51

2.6.2 I-V Measurement 52

2.6.3 IR and Optical Characterization 53

2.6.3(a) Responsivity ($\Re$) 54

2.6.3(b) Signal-to-Noise Ratio (SNR) 55

2.6.3(c) Noise Equivalent Power (NEP) 56

2.6.3(d) Normalized Detectivity (D^*) 56

2.7 Summary 57

CHAPTER THREE: FABRICATION TECHNIQUES AND DESIGN IMPLEMENTATION

3.1 Introduction 60

3.2 Fabrication Techniques Characterization 60

  3.2.1 Wafer Preparation 60

    3.2.1(a) Organic and Particles Clean(RCA-1) 61

    3.2.1(b) Oxide Strip Removal 62

    3.2.1(c) Ionic Removal (RCA-2) 62

  3.2.2 Lithography Techniques 63

  3.2.3 Photolithography 63

    3.2.3(a) Photo Plate Mask Preparation 64

    3.2.3(b) Photoresist and UV Exposure 65

  3.2.4 Electron Beam Lithography (EBL) 67

    3.2.4(a) Electron Beam Resist 68

    3.2.4(b) Exposure Parameters 69

  3.2.5 Etching Techniques 70

    3.2.5(a) Xenon Difluoride Etching 70

    3.2.5(b) Reactive Ion Etching 71

  3.2.6 Film Sputtering Deposition 73

3.3 Design and Implementation 74

  3.3.1 Material Selection 77

    3.3.1(a) Wafer of choice 77

    3.3.1(b) Metal Selection 78

3.3.1(c) Bolometer Selection 79
3.3.2 Dielectric Standoff Material 80
3.3.3 Structure Design 85
3.3.4 Antenna Design 85
3.3.5 Reflector Design 87
3.4 Fabrication Process Flow Design 89
3.4.1 Cavity Preparation 91
3.4.2 Cavity Filling and Standoff Layer 92
3.4.3 Lithographic Process 93
3.4.3(a) Lithography Sequence 94
3.4.3(b) Pattern Definition 96
3.4.3(c) Photolithography Patterns 96
3.4.3(d) EBL Patterns 96
3.4.3(e) EBL Alignment 99
3.4.3(f) EBL Automation 100
3.5 Summary 103

CHAPTER FOUR: RESULTS AND DISCUSSION

4.1 Introduction 104
4.2 Cavity Etching Analysis 105
4.3 Surface Morphology 110
4.4 SEM Measurement 114
4.5 Device I-V Measurement 116
4.6 Statistical Analysis and Discussion 118
4.7 Summary 123

CHAPTER FIVE: CONCLUSION

5.1 Future Work 126

REFERENCES 128

APPENDICES

Appendix A: SU8 Photoresist

Appendix B: EBeam Resist

Appendix C: EDX Measurement

Appendix D: Photolithography Masks

Appendix E: Fabrication Facilities

Appendix F: EBL Automation Code

LIST OF PUBLICATIONS

LIST OF TABLES

		Page
Table 2.1	Temperature coefficient of resistance of some materials (Han, 2006)	47
Table 2.2	Summary of different designs presented in the literature and their contributions	59
Table 3.1	Summary of wafer cleaning procedure	63
Table 3.2	Summary of emulsion mask preparation	64
Table 3.3	Summary of photolithography process details of SU8-2002 for 2.2 μm	66
Table 3.4	Summary of photolithography process details of SU8-10 used for permanent cavity filling	67
Table 3.5	Summary of EBL process details of bi-layer 520 nm	70
Table 3.6	Summary of a recommended etching process recipe	72
Table 3.7	Summary of RIE etching parameters	73
Table 3.8	Summary of sputtered films	75
Table 3.9	Details of focal point height calculation for samples with best cavity etching profile. (All dimensions in μm).	88
Table 4.1	Details of etching process for some of the etched samples with all dimensions in μm and gas pressure 3 Torr unless otherwise stated	105
Table 4.2	Loading details and associated etched volume according to the preferred recipe for sample S25	107
Table 4.3	Loading details and associated etched volume according to the preferred recipe for samples S21 to S25	108
Table 4.4	AFM Measurements summary	114

LIST OF FIGURES

Page

Figure 1.1 Some IR applications:(a) Surveillance, (b) Firefighting, (c) Medicine, (d) Nightvision, (e) Maintenance 2

Figure 1.2 Scanning electron micrograph of a dipole antenna-coupled infrared detector example: (a) antenna-coupled MOM diode (J. A. Bean, Weeks, & Boreman, 2011), (b) antenna-coupled bolometer (González & Boreman, 2005) 4

Figure 2.1 Some previously implemented detectors: (a) Dipole/-MOM diode, (b) Dual batch/bolometer, (c) Dipole microstrip/bolometer, (d) Bow-tie/MOM diode, (e) Spiral/-MOM dipole, (f) Log-periodic/bolometer, (g) Square spiral/bolometer, (h) Two dipole phased array/bolometer, (i) Tapered slot/MOM diode 13

Figure 2.2 Sketch of main steps for standard EBL and FIB patterning example (Biagioni, Huang, & Hecht, 2012) 15

Figure 2.3 Sketch of main steps for standard NIL and UV-NIL patterning example (Khairudin, 2009) 16

Figure 2.4 Cross-section of a patterned sample showing the undercut formation in a bi-layer resist 17

Figure 2.5 Anisotropic vs isotropic etching 20

Figure 2.6 Isotropic etching of *Si* <100> in KOH 21

Figure 2.7 Resonant dipole patterns on a semi-infinite dielectric substrate with $\varepsilon_r = 4$ and $\varepsilon_r = 12$ (Rebeiz, 1992; Rutledge & Muha, 1982) 26

Figure 2.8 Polarization ratio of Al/AlOx/Pt ACMOMDs as a function of the length of the dipole antenna (J. A. Bean, Tiwari, et al., 2010) 29

Figure 2.9 Response of tunable antenna coupled IR detector for different tuning voltages (G. D. Boreman, Cordreanu, Fumeaux, Gritz, & Christodoulou, 2001) 29

Figure 2.10 Ray illustration of trapped surface waves excitation in a substrate (C. T. Middlebrook, 2007) 31

Figure 2.11 Cavity backed structure (J. A. Bean, 2008) 32

Figure 2.12 Effective collection area enhancement approaches: (a) Antenna array in serial configuration (Mandviwala, Lail, & Boreman, 2005), (b) Antenna array in parallel configuration (G. Boreman, Gonzalez, Gritz, Codreanu, & Fumeaux, 2002) 35

Figure 2.13 Effective area increase approaches: (a) Two elements phased array (Slovick, Bean, & Boreman, 2011), (b) Fresnel zone structure (González, Alda, Ilic, & Boreman, 2004) 36

Figure 2.14 Frequency selective surface using slot antenna coupled to MOM diode (Kinzel et al., 2013) 36

Figure 2.15 Paraboloid reflector analysis (Balanis, 2005) 38

Figure 2.16 Examples of some different sensing techniques: (a) thermocouple, (b) geometric diode, (c) Schottky diode representation (top) and fabricated device before ITO coating (bottom) 39

Figure 2.17 Energy band diagram for MOM contact: (a) barrier formation, (b) trapezoidal shaped barrier due to biasing effect 41

Figure 2.18 Equivalent-circuit model of an antenna-coupled MOM diode 45

Figure 2.19 Air-bridge for isolation (Codreanu & Boreman, 2002): (a) bolometer and antenna suspended on the air, (b) suspended bolometer only 49

Figure 2.20 IR measurement setup (C. T. Middlebrook, 2007) 54

Figure 3.1 Complete device fabrication process 61

Figure 3.2 Example for one successfully transferred pattern for contact pads 66

Figure 3.3 Electrical conductivity of antenna metals from 8 to 12 μm from ellipsometer measurements (C. F. Middleton & Boreman, 2006) 79

Figure 3.4 The effect of non-flat surface of the cavity filling 82

Figure 3.5 Optical constants for *BCB* and other spin on polymers at IR band (Folks, Ginn, Shelton, Tharp, & Boreman, 2008): (a) Real refractive index, (b) Extinction factor 83

Figure 3.6 Optical constants for different lithographic resists at IR band (Folks et al., 2008): (a) Real refractive index, (b) Extinction factor 83

Figure 3.7 Parabolic reflector front (left) and side view cross section (right) 85

Figure 3.8 Summary of the range of calculated dimensions for the designed dipole antenna 87

Figure 3.9 Substrate preparation process flow: (a) Cavity structure etching, (b) Cavity filling 90

Figure 3.10 Detailed lithography sequence, cross sectional view (left) and top view (right) 95

Figure 3.11 Single chip details : (a) The dot pattern for cavity micromachining, (b) Bonding Pads 97

Figure 3.12 Beam calibration before exposure 98

Figure 3.13 Designed GDSII file representing bolometer and alignment marks 99

Figure 3.14 Designed GDSII file representing dipole antenna and leadlines 100

Figure 3.15 Alignment Marks Set: (a) Single marker, (b) 4 markers set at upper right corner 101

Figure 3.16 EBL semiautomated process flow 102

Figure 4.1 Micrograph of the implemented structure through process flow defined in Section 3.4 104

Figure 4.2 Profile measurement for etched parabola with the mask included: (a) Top view for patterned surface, (b) Cross section measurement 106

Figure 4.3 Profile measurement for etched parabola after removing the mask: (a) Top view for patterned surface, (b) Cross section measurement 106

Figure 4.4 Etching analysis showing effect of increasing number of cycles: (a) 3 cycles (S21), (b) 4 cycles (S22), (c) 5 cycles (S23), (d) Surface profile comparison: S21 with 3 cycles (red), S22 with 4 cycles (magenta), and S23 with 5 cycles (cyan) 109

Figure 4.5 Surface profile comparison with increasing number of cycles after prolonged storage under vacuum: (a) S24 with 4 cycles (green), (b) S25 with 5 cycles (blue) 110

Figure 4.6 Cavity SU8-10 filling : (a) Surface top view, (b) Profile analysis 111

Figure 4.7 Patterned bolometer after development: (a) Top view for patterned 450 *nm* × 750 *nm* bolometer, (b) Profile analysis showing a bolometer length of 750 *nm* (brown) and width of 550 *nm* (blue) 112

Figure 4.8 Patterned antenna arms after development: (a) Top view for patterned arms, (b) Profile analysis showing a dipole width of 350 *nm* (brown) and leadline width of 260 *nm* (blue) 113

Figure 4.9 SEM image for the completed device 114

Figure 4.10 SEM measurement for metallic deposited patterns after liftoff processes: (a) Nb bolometer, (b) Aligned Au antenna arms on bolometer 115

Figure 4.11 I-V measurement setup: (a) Probes on the sample, (b) Device under test 116

Figure 4.12 IV characteristics measurement for a completed device 117

Figure 4.13 Statistical analysis for the showing the damaged and failure during sample preparation for EBL process 119

Figure 4.14 Device misalignment results in device discontinuity 121

Figure 4.15 Effect of resist residuals on liftoff and device continuity: (a) Top view for a measured antenna, (b) Antenna profile analysis 122

Figure A.1 SU8-10 thickness profile vs spin coating speed 138

Figure A.2 SU8-2002 thickness profile vs spin coating speed 138

Figure B.1 PMMA thickness profile vs spin coating speed 139

Figure B.2 Copolymer thickness profile vs spin coating speed 139

Figure C.1 EDX measurement for the gold sputtering target used in the project 140

Figure D.1 Complete bonding pads pattern set divided into 4 groups of chips 142

Figure D.2 Alignment marks details : (a) Generic marks, (b) Spacing to nearest chip corner 142

Figure E.1 Photo of LA410o2 mask aligner 143

Figure E.2 Photo of MM605 mask fabrication machine 143

Figure E.3 EBL System : (a) Simplified generic block diagram, (b) JEOL JSM-6460-LV SEM outfitted with Raith Elphy quantum universal lithographic attachment 144

Figure E.4 Photo of *XACTIX e1* series xenon difluoride dry etching machine 144

Figure E.5 Reactive Ion Etching, RIE, system: (a) Simplified generic block diagram , (b) Photo of Oxford Plasmalab 80 Plus RIE/ICP system 145

Figure E.6 Sputtering deposition system: (a) Simplified generic block diagram (Raimondo, Puckett, & Webster, 2010), (b) Photo of Auto HHV500 RF and DC sputtering deposition system 145

LIST OF ABBREVIATIONS

ACMOMD	Antenna Coupled Metal-Oxide-Metal Detector
AFM	Atomic Force Microscope
Al	Aluminum
Al_2O_3	Aluminum Oxide or alumina
Ar	Argon
Au	Gold
BCB	Benzocyclobutene or Cyclotene
Bi	Bismuth
C	Heat Capacity
CF_4	Carbon Tetrafluoride
Cr	Chromium
CMOS	Complementary Metal Oxide Semiconductor
CO_2	Carbon Dioxide
CPS	Coplanar Strip
D^*	Normalized Detectivity
DC	Direct Current
DI water	Deionized water
DITI	Digital Infrared Thermal Imaging
EB	Electron Beam

EBL	Electron Beam Lithography
FWHM	Full Wave at Half Maximum
FZPL	Fresnel Zone Plate Lens
G	Thermal Conductivity
GDS	Graphic Database System
H_2O	Water
H_2O_2	Hydrogen Peroxide
HCl	Hydrochloric acid
He	Helium
HeNe	Helium Neon
HF	Hydrofluoric acid
IPA	Isopropyl Alcohol or isopropanol
IR	Infrared
LWIR	Long Wave Infrared
MCT	Mercury Cadmium Telluride
MIBK	Methyl Isobutyl Ketone
MIM	Metal Insulator Metal
MMW	Millimeter Wave
MOCVD	Metal Organic Chemical Vapor Deposition
MOM	Metal Oxide Metal
MWIR	Mid Wave Infrared

Nb	Niobium
NDF	Natural Density Filters
NEP	Noise Equivalent Power
NETD	Noise Equivalent Temperature Difference
NFM	Nano-fabrication and Functional Material
Ni	Nickel
NOR	Nano-Optoelectronic Research
O_2	Oxygen
PMMA	Polymethyl Methacrylate
RCA	Radio Corporation of America
RF	Radio Frequency
RIE	Reactive Ion Etching
rpm	revolutions per minute
sccm	standard cubic centimeters per minute
SEM	Scanning Electron Microscope
Si	Silicon
SiF_4	Silicon tetrafluoride
SiO_2	Silicon Dioxide
Si_3N_4	Silicon Nitride
SNR	Signal to Noise Ratio
TCR	Temperature Coefficient of Resistance

THZ	Terahertz
VO_x	Vanadium Oxide
VSWR	Voltage Standing Wave Ratio
USM	Universiti Sains Malaysia
W	Tungsten
XeF_2	Xenon Difluoride
ZnSe	Zinc Selenide

REKA BENTUK DAN FABRIKASI PENGESAN INFRAMERAH GANDINGAN NANO-ANTENA DENGAN PEMANTUL PARABOLA

ABSTRAK

Tesis ini memberi tumpuan ke atas proses reka bentuk dan fabrikasi pengesan inframerah (IR) gandingan bersepadu nano-antena dengan pemantul parabola yang novel. Oleh kerana peranti ini berasal dari antena yang digabungkan dengan pengesan IR, ia menawarkan kelebihan dari segi tindak balas yang pantas, tidak memerlukan keadaan yang sejuk untuk beroperasi, pemilihan frekuensi, kepekaan polarisasi dan keserasian CMOS. Walau bagaimanapun, teknik fabrikasi yang mencabar telah membatasi penyelidik dalam banyak aspek. Kebanyakan penyelidikan dalam literatur hanya terhad kepada reka bentuk antena 2D sahaja. Pembangunan proses fabrikasi melalui pemesinan mikro 3D boleh menambah lebih banyak jenis struktur antena gandaan tinggi 3D seperti mana antena pemantul parabola yang dicadangkan dalam tesis ini. Struktur sedemikian secara teori dijangka meningkatkan kepelbagaian ruang gandaan dan mengurangkan kehilangan mod substrat. Oleh itu, struktur baru ini mempunyai potensi yang tinggi untuk meningkatkan kecekapan alat-alat pengesanan dan membuka jalan ke arah pengkomersialan. Proses fabrikasi dibentangkan dan dioptimumkan dalam tesis ini terutamanya EBL automatik dan XeF_2 punaran. Struktur ini direka bentuk dengan tujuh lapisan antena suapan dwikutub gelombang 4.2 μm untuk operasi dalam jalur inframerah gelombang panjang (LWIR) pada gelombang jarak 10.6 μm tergandingan dengan kelompok niobium 450 $nm \times 750$ nm sebagai bolometrik setempat penderia. Foto-berintangan SU8-10 digunakan sebagai pengisian dan rongga rata yang berkos rendah. Analisis morfologi telah menunjukkan perbezaan ketinggian kurang daripada 400 nm di atas keseluruhan bukaan. Rongga parabola bersepadu secara purata mempunyai 75 μm diameter bukaan dan 13 μm kedalaman rongga. Resipi punaran iaitu 5 kitaran dengan 30 s setiap kitaran pada tekanan gas punaran 3 Torr telah digunakan untuk analisis punaran XeF_2. Resipi ini membuat punaran dengan 0.3425 mm^3 isipadu yang memerlukan profil rongga 2.2 μm SU8 topeng sebagai 38 μm diameter pekeliling corak tingkap utama dan beberapa penanda yang mewakili 3.7122 mm^2 kawasan bercorak. Analisis geometri untuk mencirikan proses fabrikasi telah dibentangkan dan SEM struktur akhir telah mencapai reka bentuk yang dicadangkan. Walau bagaimanapun, pengukuran I-V menunjukkan ciri-ciri tidak linear dengan kerintangan yang sangat tinggi iaitu sebanyak 222 $k\Omega$. Ini menghalang jalan ke arah pengkomersialan alat-alat fabrikasi untuk kegunaan ukuran optik. Masalah ini dirujuk kepada proses lepas-angkat yang tidak bersih kerana menyebabkan kekacauan di atas semua lapisan peranti yang dibuat. Perbincangan terperinci dengan bantuan analisis statistik telah dibentangkan. Proses fabrikasi peranti ini dibentangkan dengan jayanya termasuk teknik pemesinan mikro dan teknik corak, tetapi lebih banyak usaha diperlukan untuk penyelidikan pada masa depan bagi mengatasi masalah yang diketengahkan dan memperkenalkan peranti yang diusulkan ke pasaran.

DESIGN AND FABRICATION OF INTEGRATED PARABOLIC REFLECTOR NANO-ANTENNA COUPLED INFRARED DETECTOR

ABSTRACT

This work focuses upon the design and fabrication process of a novel parabolic reflector integrated nano-antenna coupled Infrared (IR) detector which is presented here for the first time. As this device stems from antenna coupled IR detectors, it will still also offer the advantages of the fast response, uncooled operation, frequency selectivity, polarization sensitivity and CMOS compatibility. However, the challenging fabrication techniques limited researchers' work in many aspects. Most of the research in the literature was thus confined to 2D antenna design only, while developing the fabrication process through 3D micro-machining can add more varieties of 3D high gain antenna structure such as the parabolic reflector antenna proposed through this work. Such a structure is theoretically expected to add a space diversity gain and reduce the substrate mode losses. Therefore, the new structure has a high promising potential for efficiently increasing the specific detectivity of these devices paving the way towards commercialization. The fabrication process is presented and optimized through this work facilitated mainly by automated EBL and XeF_2 etching. The structure is designed of seven layers encountering a 4.2 μm half wave dipole feeding antenna for operation in the long wave infrared band (LWIR) at wavelength 10.6 μm coupled with a 450 $nm \times 750$ nm niobium batch as a sub-wavelength localized bolometric sensor. The SU8-10 photoresist is used permanently for low cost insulating and flat cavity filling purposes showing a height variation of less than 400 nm over the whole cavity aperture through the morphology analysis. The integrated parabolic cavity has 75 μm and 13 μm on average for its aperture diameter and cavity depth respectively. The

presented XeF_2 etching analysis reveals that, according to the proposed structure design, the proper etching recipe is described by 5 cycles, with 30 s each, at an etching gas pressure of 3 Torr. This recipe is sufficient to etch approximately a total volume of 0.3425 mm^3, resulting in the required cavity profile, through a 2.2 μm SU8 mask that provides mainly circular windows pattern of 38 μm in diameter and few markers representing a total patterned area of 3.7122 mm^2. The different geometrical analyses that are encountered for characterizing the fabrication process have been presented and the SEM of final structure has showed a good agreement with the proposed design. The I-V measurements have showed, however, non-linear characteristics with an extremely high impendence of 222 $k\Omega$ that hinder introducing the fabricated devices for the optical measurements. This problem is referred to the non-clean liftoff as it results in discontinuity of all the fabricated devices' layers. A detailed discussion with the aid of the statistical analysis had been finally presented. The fabrication process of this device is thus presented successfully including micro-machining and patterning techniques, but more efforts can be encountered in the future work to overcome the highlighted issues and introduce the proposed device to the field.

CHAPTER ONE

INTRODUCTION

1.1 Infrared Detection

Since the first time it had emerged during the second world war, Infrared (IR) detection and imaging at wavelengths of the two atmospheric windows of 3 to 5 and 8 to 14 μm has been extensively researched. Many generations of these detectors have been developed to accommodate various applications in different fields such as military, space, science, medicine, engineering and industry. Figure 1.1(a,b,c,d) catalogs the effectiveness of using IR imaging compared to normal imaging in some real applications such as surveillance and security, firefighting and medical imaging. Figure 1.1(e) also shows the use of IR imaging to detect the high current flow for predictive maintenance.

A wide range of various other applications have also been developed, such as mine detection, industrial process control and terahertz (THz) and infrared spectroscopy (J. A. Bean, Tiwari, et al., 2010; Kanwano, 2012; Niklaus et al., 2007). More recently IR detectors have also been proposed for energy harvesting applications, attracting more attention of many researchers (Gragnani & Bergamaschi, 2017; Meredov et al., 2017; Shao et al., 2012). To unlock more potential applications, detection without requirements for cooling was previously desired such that the required bulky and expensive cryogenic cooling equipment can be eliminated exploiting consequently more applications via compact and low cost solutions.

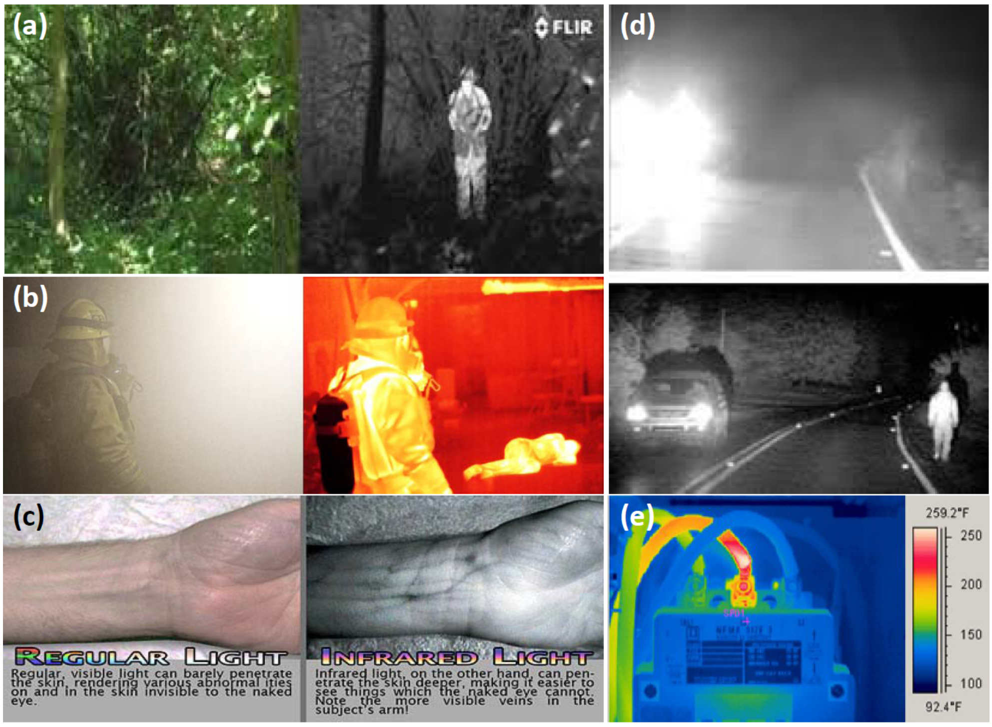

Regular, visible light can barely penetrate the skin, rendering various abnormal ities on and in the skin invisible to the naked eye.

Infrared light, on the other hand, can penetrate the skin deeper, making it easier to see things which the naked eye cannot. Note the more visible veins in the subject's arm!

Figure 1.1: Some IR applications:(a) Surveillance, (b) Firefighting, (c) Medicine, (d) Nightvision, (e) Maintenance

Similarly, along with the removal of cooling requirements for detection, the high speed detection as well as spectral selectivity are now reported as the main required features for the new generation of these detectors. The development of the high speed detectors paved the way to high frame rate cameras which offer a good solution for many critical applications such as target detection, tracking and navigation in autonomous vehicles. Moreover, with the spectral selectivity, dual-band cameras are achievable enabling clutter suppressed enhanced imaging applications such as missile warning systems to be more reliable (Breiter et al., 2002). Also, multi-spectral detection is beneficial for THz and infrared spectroscopy applications for chemical detection and materials characterization (Dong et al., 2017; Weber et al., 2017).

For the new generations proposed recently therefore, the main required features are to achieve high speed detection with spectral and polarization selectivity while operating at room temperature as well. Nano-antenna coupled IR detectors have thus received a great interest from researchers as a promising candidate that can fulfill these requirements (González & Boreman, 2005; Grover et al., 2010).

1.2 Nano-Antenna Coupled IR Detectors

By exploiting the wave nature of light, the nano-antenna coupled detectors have been introduced as a new member in the IR detectors family. The nano-antenna, which operates in the THz regime, is conceptually used to optimize the energy transfer from the freely propagating radiation field to a localized sensor which became much smaller than the wavelength (Donchev et al., 2014; Novotny & Van Hulst, 2011). The ultra-fast response as well as the uncooled operation capability are both referred back to the submicron size of the sensor. The nano-antenna also offers spectral selectivity as well as polarization sensitivity that are the inherent advantages that can eliminate the heavy bulky optical filters and polarizers, in the order of more than 1 kg, required for previous commercial bolometric focal plane array IR cameras (G. Boreman et al., 2002). Moreover, CMOS compatibility, extremely low design profile of these devices as well as the simplicity of the hardware circuit required gave these detectors extra attractive advantages thus increasing the interest of researchers in such devices (J. A. Bean, Tiwari, et al., 2010). Antenna coupled IR detectors, such as antenna coupled bolometers (González & Boreman, 2005; P. Krenz et al., 2008; C. T. Middlebrook et al., 2008) and antenna-coupled rectifiers (AbdelRahman et al., 2004; J. A. Bean, Tiwari, et al., 2010; J. A. Bean et al., 2011; Codreanu et al., 2003; Fumeaux et al., 1998), have therefore received great interest from researchers. An example of the antenna coupled metal-oxide-metal (ACMOMD) as well as the antenna coupled bolometer detectors are shown in Figure 1.2.

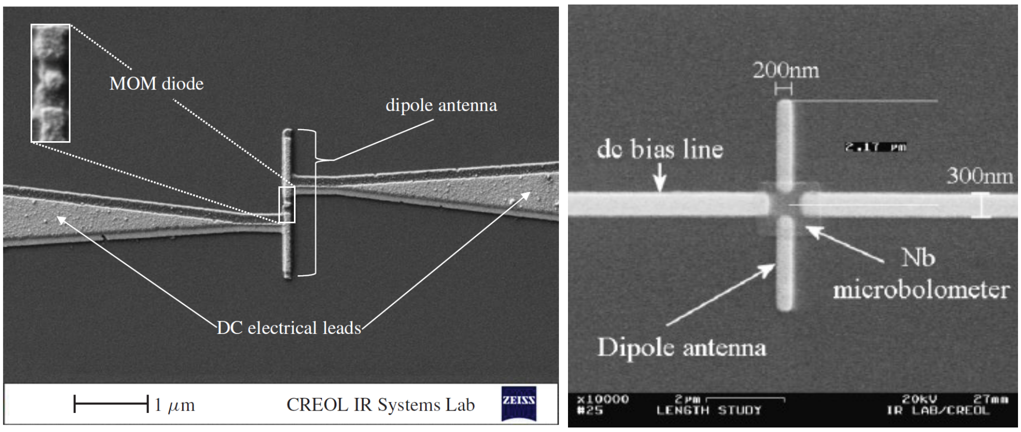

(a) (b)

Figure 1.2: Scanning electron micrograph of a dipole antenna-coupled infrared detector example: (a) antenna-coupled MOM diode (J. A. Bean et al., 2011), (b) antenna-coupled bolometer (González & Boreman, 2005)

Although many other competitors had been already employed and can offer applicable solutions to meet the new generation's required features, some encountered difficulties and problems had limited the availability and manufacturing yield of these detectors. The critical epitaxial growth of mercury-based compounds required for the Mercury Cadmium Telluride (MCT) detectors as well as air bridge and suspended structures required for the bolometric focal plane array are two examples of these difficulties in fabrication (Krishna et al., 2007).

1.3 Statement of the Problem

Due to the presence of the supporting substrate for the nano-antenna, both air-dielectric interface in addition to the new optical and electrical materials' parameters at the IR band result in performance degradation in antenna coupling efficiency and the whole device performance in its turn. Accordingly, power loss due to substrate modes, attenuation due to surface impedance and Coleman effects are all present (J. A. Bean, Tiwari, et al., 2010; Wilke, Herrmann, & Kneubühl, 1994). This limited the performance of these devices, in terms of the detectivity as the common figure of merits, to be three orders of magnitude lower than their cryogenic-cooled IR counterparts (AbdelRahman & Kusuma, 2010).

Considerable efforts had been made to improve the overall efficiency of the device either by increasing antenna coupling efficiency (J. A. Bean et al., 2011; Florence et al., 2011; Fumeaux et al., 2000; González & Boreman, 2005; C. T. Middlebrook et al., 2008; Shelton et al., 2008), sensing device efficiency (J. A. Bean et al., 2008, 2011; Fumeaux et al., 1998), impedance matching efficiency between both the antenna and the sensing device (Grover et al., 2010; P. M. Krenz et al., 2012) or even optimizing the fabrication process (Bareib et al., 2011; J. A. Bean et al., 2011). However, due to the great challenges in the nano-fabrication techniques, all the conducted research had been constrained to 2D antenna structures.

Developing the fabrication process to accommodate 3D antenna structures is thus promising as it will pave the way for implementing different high gain antenna designs and integrating cavities at the back of antenna. Such integration is potentially required to eliminate the substrate mode losses (Balanis, 2005), that had been reported to result in loss up to 90% (Rebeiz, 1992), and thus enhance the device performance in its turn. It was equally important, however, that the new structure should also maintain the device CMOS compatibility as well as the simplicity of its profile such that it can be easily commercialized.

A cavity backed structure can confine the surface waves and prevents them from propagating away of antenna. This will thus reduce the substrate modes losses and enhance the response as well due to resonance in the cavity (J. A. Bean, 2008). A rectangular cavity backed structure had been previously implemented in millimeter wave (MMW) band (Sun & Fay, 2006), but yet without any steps toward implementation in IR band due to the finest dimensions and the resultant difficulties in fabrication process imposed at the IR band. However, with the aid of 3D micro-machining and isotropic etching techniques, a micro-parabolic cavity can be introduced. The parabolic cavity is expected to coherently confine the waves at the antenna when it is properly aligned to the focal point (Sletten, 1988). In this case, a high gain with very low side lobes and pencil beam is then achievable (Balanis, 2005). Moreover, the parabolic reflector can also offer a high polarization discrimination response, which is useful and important for many applications such as clutter suppressed as well as high resolution imaging applications. The parabolic reflector, in general, will also result in an increased effective antenna aperture area that will add a space diversity gain to the detector.

1.4 Research Objectives

This work is confined to develop the nano-fabrication process to implement a 3D nano-antenna structure. Drawing inspiration from the radio frequency regime, the novel parabolic reflector integrated structure is proposed in this project as a promising structure with a high expectation to increase the detectivity of these devices. In summary, this research is focused mainly to achieve the following objectives:

1. To design the parabolic reflector integrated antenna coupled IR detector.

2. To characterize and optimize the fabrication process as well as the materials required according to the designed structure required geometry as well as materials availability.

3. To fabricate the designed parabolic reflector integrated structure.

1.5 Scope and Limitations

The scope of this work is therefore focused only upon design and fabrication of a parabolic cavity integrated with a half wavelength nano-dipole antenna coupled bolometer. The optical measurement of the fabricated devices is not included in the scope of this work. The fabrication of the proposed device is achieved and mainly facilitated by the use of a JEOL/Raith quantum electron beam lithography for nano size antenna while the cavity etching is carried out using the *XACTIX e1* series isotropic xenon difluoride etching machine. These machines are offered in USM in the Nano-Optoelectronic Research (NOR) laboratory at the School of Physics, Collaborative Micro-Electronic Design Excellence Centre (CEDEC), and the Nano-fabrication and Functional Material (NFM) laboratory at the School of Mechanical Engineering.

1.6 Thesis Outline

In this thesis, the research work is outlined as follows: Chapter 2 presents the theoretical background of nano-antenna coupled devices. Brief descriptions of the main concepts of these devices are summarized. The challenging issues of the different design parameters are outlined. The previous attempts in these regards as well as the historically researched issues are reviewed. Chapter 3 presents an overview for the different micro/nano-fabrication available facilities in USM that are utilized in this research. The detailed recipe for each process that was used for the proposed design in particular is tabulated. The detailed model design and implementation details will then follow. Chapter 4 presents the findings of this research. The measurements of the implemented detectors are thus documented. A statistical analysis has been then presented and the different encountered problems as well as their solutions are all discussed accordingly. Chapter 5 provides the conclusion of this research work with a summary of the important findings and accomplishments.

CHAPTER TWO

RESEARCH BACKGROUND

2.1 Introduction

Both the long wave infrared (LWIR) band, that is ranging between 8 to 14 μm and the mid wave infrared (MWIR), that is ranging between 3 to 5 μm, are becoming increasingly important for various commercial and military applications. The importance of these bands comes as a result of being strongly emitted by objects near 300 K and 500 K respectively. These objects will include human bodies, animals, trees and other heat sources, such as engines, vehicles and machinery (J. A. Bean, Tiwari, et al., 2010). Moreover, their relatively low absorption in the atmospheric window added more special interest in designing and developing detectors in these bands for different imaging applications. The longer wavelength is attractive for its higher sensitivity, whereas shorter one is more attractive for higher contrast imaging purposes (Rogalski, 2002).

These detectors will have many applications for the majority of commercial and military infrared applications. Infrared imaging is one of the most common infrared detection applications with the greatest potential such as night vision systems that are used for military purposes. The Digital Infrared Thermal Imaging (DITI) system had been originally designed for this purpose by the US military. Moreover, this technology had been also employed for target detection, tracking and navigation in autonomous vehicles. Its ability to image the scenes that are invisible to the naked eye unlocks huge potential applications for reconnaissance, surveillance and firefighting. Another wave of applications are commercially explored for mine detection, predictive maintenance and industrial process control (J. A. Bean, Tiwari, et al., 2010; Niklaus et al., 2007). Using IR detectors for energy harvesting applications recently attracted the attention of many researchers (Shao et al., 2012). Also, Terahertz and infrared spectroscopy application is well established for powerful characterization of the physical and chemical properties for various materials (Kanwano, 2012). In medical science also, this technology has significant impact that makes it likely to surge soon. The IR detection applications in medical imaging offers non-contact, non-invasive, ultra-fast, painless and safe imaging that is useful in screening, diagnosis, analysis, follow up and assessment after treatment or even thermal load evaluation during surgery for various medical areas. It had been extensively researched for a wide range of applications starting from simple fever monitoring, blood pressure monitoring, tumor detection, including also applications in dentistry, dermatology, orthopedics, rheumatology to gynecology, as well as ophthalmology, and even thermoencephaloscopy for brain imaging (Antonina Calin et al., 2015; Arora et al., 2008; Flores-Sahagun et al., 2011; Lahiri et al., 2012).

One of the state of the art detectors is the antenna coupled detector. The general structure of these detectors is composed of two main elements: nano-antenna as a collection element and a sensing element. The nano-antenna can efficiently link the propagating and spatially localized optical fields , resulting in a proportional induced current in antenna arms, which in its turn will be applied to the sensing element hence the name "antenna coupled detector". The most commonly used sensing elements will then sense the alternating signal at THz frequencies either by a bolometric or rectification technique. The antenna offers spectral selectivity as well as polarization sensitivity that are the inherent advantages that can eliminate the bulky optical filters and polarizers required for previous commercial bolometric focal plane array IR cameras. The separation of the power harvesting and sensing functions of the detector allows for sensor dimensions much smaller than the wavelength which will result in a detector with high speed, low noise, and room temperature operation. Due to separation between power harvesting and sensing functions, optimization of both functions independently will lead to numerous possible combinations of shapes and materials for both the sensor and its antenna (Fumeaux et al., 2000). Moreover, with the capability of function at room temperature, the elimination of cryogenic cooling will make the system much cheaper and very compact. Even with the relatively low specific detectivity (D*) of these detectors compared to their competitors, these detectors are low profile and CMOS compatible (J. A. Bean, Tiwari, et al., 2010). When compared to either the bolometeric focal plane array with the difficulty of air suspension implementation or the Mercury Cadmium Telluride (MCT) detectors and the required critical epitaxial growth of mercury-based compounds (Krishna et al., 2007), these detectors seem attractive to many authors and worth the efforts to increase its detectivity.

Some of the different configurations of these detectors that had been previously implemented in the literature are illustrated in Figure 2.1. The chronological development of these devices started for the first time in the 1960s by point-contact or cat whisker diodes which were capable of functioning as infrared detectors (J. A. Bean, Tiwari, et al., 2010). Lithographic antenna-coupled infrared detectors had been then introduced during the mid-1970s making these devices more rugged, shock proof and reproducible (Codreanu et al., 2003; Wilke, Oppliger, et al., 1994). The application of these detectors in the mid-IR band was first addressed by Grossman et al.

(1991) who had implemented a spiral antenna coupled to a *Nb* bolometer for 9.5μm wavelength detection. The dipole antenna was commonly proposed and used by different researchers for its simplicity. Wilke, Herrmann, and Kneubühl (1994) studied experimentally a simple dipole ACMOM in a wide range of dipole lengths as well as different substrate layer thickness. It was the first time the use of a quarter wave length matching substrate thickness was proposed. Other innovations have included work done by Chong and Ahmed (1997) where they fabricated both log-periodic and bow-tie antenna coupled bolometer detectors. Fumeaux et al. (1998) demonstrated both the spiral and bow-tie antenna coupled to MOM diodes. Codreanu and Boreman (1999) reported a microstrip patch antenna coupled to a bolometer. One year later, they repeated again the resonance length measurement for a simple dipole coupled to a bolometer for LWIR and MWIR as well as visible band (Fumeaux et al., 2000). Codreanu and Boreman (2001) published microstrip dipole antennas coupled to niobium micro-bolometers. Bulls eye antenna also coupled to cryogenic quantum dot photodetector for IR detection was developed by Lee et al. (2006). Integrating nano-antenna arrays to a colloidal quantum dot based photodetector designed for mid-IR to enhance the photocurrent was also introduced (Yifat et al., 2017). Phased antenna array was first demonstrated by C. T. Middlebrook (2007). The linear tapered slot antenna was also demonstrated by Florence et al. (2011). The bow-tie antenna was again demonstrated coupled to a graphene diode by Zhu et al. (2013).

In this chapter, a review on nano-antenna coupled detectors will be provided. Due to the significant dependence of these detectors' performance on the structure geometry, the critical device fabrication issues and techniques required through this project are thus presented first. To provide a solid background, the general consideration for

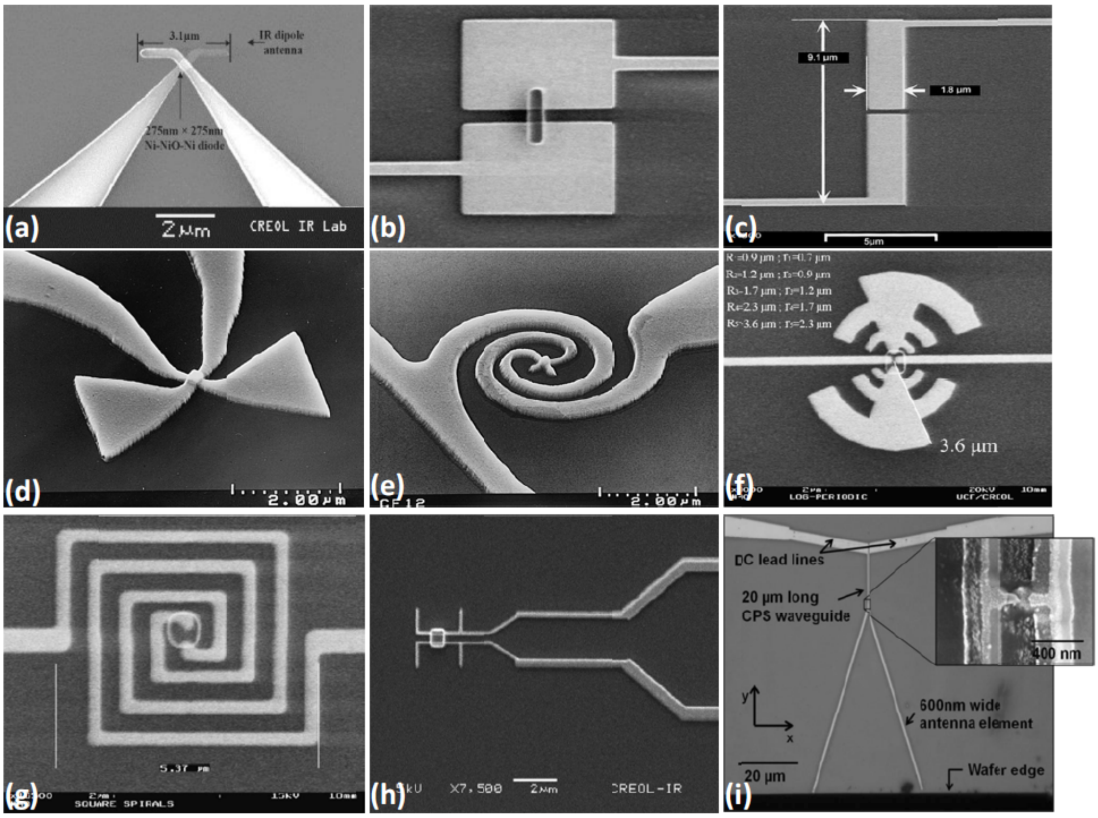

Figure 2.1: Some previously implemented detectors: (a) Dipole/MOM diode, (b) Dual batch/bolometer, (c) Dipole microstrip/bolometer, (d) Bow-tie/MOM diode, (e) Spiral/MOM dipole, (f) Log-periodic/bolometer, (g) Square spiral/bolometer, (h) Two dipole phased array/bolometer, (i) Tapered slot/MOM diode

designing these detectors will be investigated. In this context, both antenna and the coupled localized sensing elements will be discussed individually. The matching techniques between both elements will be also investigated. A brief description of the figure of merit of these detectors and the various measurements that may be encountered will be finally highlighted.

2.2 Device Fabrication

Device fabrication techniques is the most crucial issue of concern for the proper development of these detectors. Different aspects and challenging requirements in the fabrication techniques had been investigated in the literature taking into account the target applications as well. In general, to enable study, analysis and comparison for different detector configurations, the major challenging issue is the reliable and the reproducible structuring with the required high resolution. Moreover, other different considerations through the process, including mainly either increasing the integrity, reducing the implementation complexity, or even enhancing the overall performance, were all addressed. For example, whenever these devices are required to be implemented in arrays for IR imagers and cameras as well as energy harvesters, the fabrication process that can accommodate the high dense large integration is thus required. In such cases, the lithographic techniques that can achieve high resolutions that is sufficient for patterning a MOM diode with a contact area of 0.01 μm^2, as an example, were mandatory for the development of these detectors.

2.2.1 Nano Lithography Techniques

For antenna design at the IR and optical wavelengths, the antenna dimensions are required to be in the range of few hundred nanometers. Therefore reliable patterning techniques of a very precise nano structures are highly considered. The antenna resonance and the field concentration are both strongly dependant on antenna arm length as well as the feed gap size. Nano lithography techniques are thus the main key factor to accomplish the well-defined structures in the nanometer dimensions. Fabrication techniques that have been demonstrated to be effective for this purpose include electron beam lithography (EBL), focused ion beam (FIB) milling, nano-imprint lithography (NIL) (Bareib et al., 2011), and colloidal lithography (Chen et al., 2017).

The EBL and FIB are both categorized as top-down approaches that offer sequential patterning on a flat substrate. EBL, which is most popular technique, uses a controlled focused beam of highly energetic electrons to expose and develop a high resolution E-beam sensitive resist according to a designed pattern.

On the other hand, FIB is based on localized nano spots sputtering of a conductive material using a focused and accelerated Gallium (Ga) ions knocking off the atoms of the metal. The FIB offers advantage over EBL as it can achieve nanometer patterns without using any resist for lithography. However, FIB shows some probability of contamination due to redepositing of the milled atoms as well as Ga ion implantation into patterned structure. Furthermore, it usually results in a structure walls of a tapered shape causing a non-uniform structure cross section, the effect that is less pronounced for EBL (Biagioni et al., 2012). Both techniques are simply described in Figure 2.2

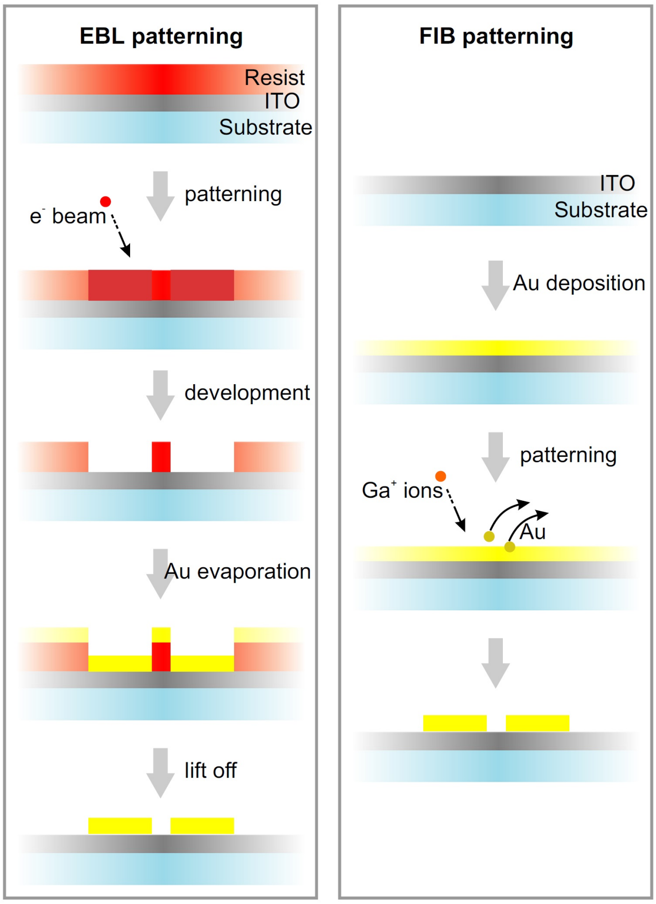

Figure 2.2: Sketch of main steps for standard EBL and FIB patterning example (Biagioni et al., 2012)

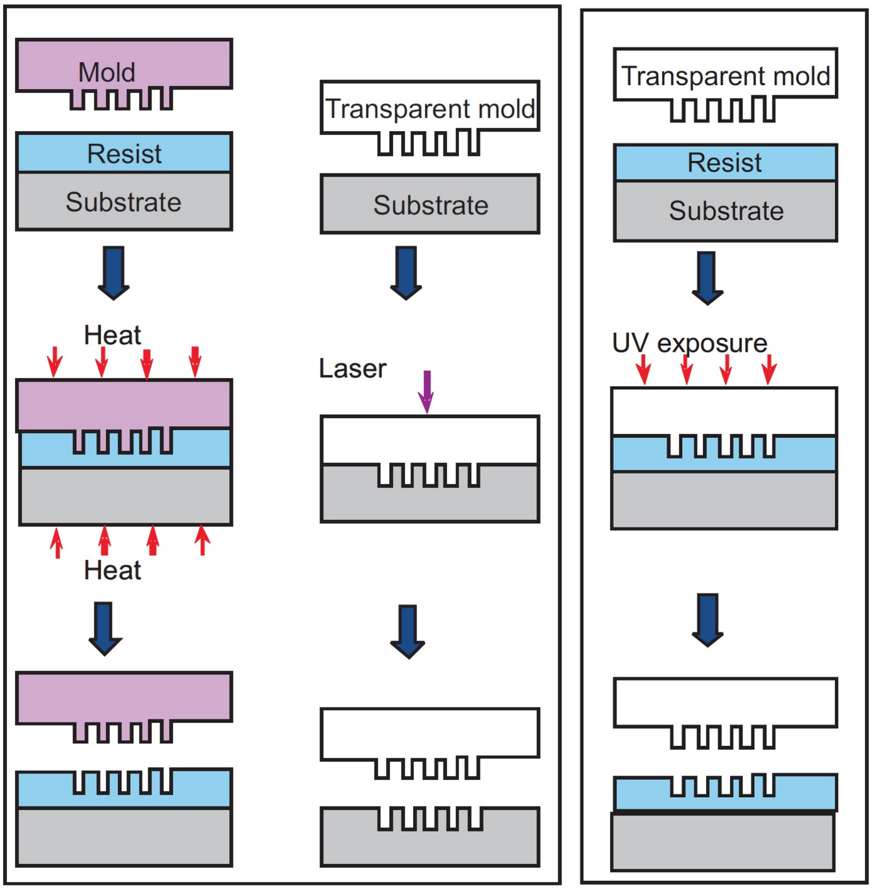

(a) (b)

Figure 2.3: Sketch of main steps for standard NIL and UV-NIL patterning example (Khairudin, 2009)

While both EBL and FIB are efficient tools for research and prototyping, but both are time consuming processes. NIL is another alternative that offers a high throughput technique and suitable for large area fabrication as well. It is based on pressing a hard mold, that includes all the surface topographic features, into a thin polymer film under controlled pressure and then cured either thermally or using UV as shown in Figure 2.3. Anyhow, NIL mask creation is the major limitation compared the the former techniques.

Figure 2.4: Cross-section of a patterned sample showing the undercut formation in a bi-layer resist

2.2.1(a) E-beam Resist and Liftoff Techniques

Although EBL is the most commonly used lithographic technique, it often involves a liftoff process, which can be restrictive in creating nano structures with high aspect ratios (Aksu et al., 2010). To ease the liftoff process, a bi-layer e-beam resist, that is composed of a high contrast resist on top of higher sensitivity resist, is frequently used. This technique introduces an undercut below sufficiently thick bi-layer resist, as illustrated in Figure2.4. This will provide a clean separation of the deposited metals on top of the resist and that in the voids, and therefore will result in higher pattern resolution as well as cleaner edged patterns. As a rule of thumb the thickness of the resist should be at least three times the thickness of the deposited film to get the best results using liftoff (González, 2003).

Polymethyl methacrylate (PMMA) and methyl methacrylate-methacrylic acid (MMA-MAA) are the most common resist pair used for bi-layer structure and frequently reported. Nevertheless, other resist pairs can be also used for the same purpose such as polydimethyl glutarimide (PMGI) ZEP 520A-7 as reported by C. F. Middleton and Boreman (2006).

It is fairly obvious of course that the optimal exposure dose will have a very significant impact on achieving the required undercut profile. Moreover, it had been found that the behavior of PMMA that may change from a positive to a negative tone if over-exposed with more than 10 times the optimal positive dose as PMMA in this case will cross-link, forming a negative resist (González, 2003).

2.2.1(b) Shadow Masking Technique

The multi-layer lithographic processes were required to implement both antenna and sensor element separately. However, with the high resolution and thin film multi-level structures,the multi-layer lithography is representing a considerable high difficulty in the device fabrication. A fabrication process with a single EBL process only is therefore preferred.

One possibility was to develop a new device structure that is employing a single metal only as reported by Szakmany et al. (2015), whereas another trend was addressed by developing the fabrication process to facilitate this need of a single lithography process. Single EBL process had been therefore addressed for ACMOMD, through applying the shadow mask technique J. A. Bean et al. (2008). Along with offering a single EBL process, this technique also enables implementation of MOM diode with smaller contact.

In the shadow mask technique, the higher speed of the copolymer is traded for the higher resolution of PMMA. The undercut in the copolymer of this process is so large that can diffuse underneath the PMMA to form free-standing bridges of PMMA. Applying a normal incidence directional deposition twice, each with a slight wafer tilting in an opposite angle to each other, will result in the formation of a very small contact area under the bridge. In addition to offering an easier fabrication process, this technique also enables the formation of the oxide layer of MOM diode under the same vacuum before introducing the second metal layer deposition. This provides thus a highly controlled oxide thickness of high quality.

2.2.2 3D Micro-machining and Etching Techniques

Advances in Si micro-machining techniques had a great impact on the development antenna coupled IR detector. For instance, with the thermal detectors implemented suspended on a membrane, the thermal conductance increased significantly and it therefore contributed for the uncooled operation.

Etching techniques are generally categorized into either dry or wet etching. While wet etching is more commonly used for its low cost, dry etching is notably advantageous over wet etching from many aspects. Mainly, as it is a gaseous phase chemical diffusion process, no sticking problems are associated or encountered. This hence leads to a more uniform etching process with excellent profile dimensional control. With the wet etching, on the other hand, the sticking problem between the freed products and the substrate, results in passivation of the surface that deteriorates the etching rate especially for the small and tinny features where the surface tension force is quite large. From an economical point of view also, dry etching is more attractive in terms of the quantity of process chemicals utilized. The elimination of wet chemicals handling and the waste disposal is certainly a notable advantage.

Among many techniques to etch silicon wafers, an isotropic etching profile is the main requirement for the cavity structure that is proposed throughout this work. As shown in Figure 2.5, the isotropic etching, which results in etching at the same or comparable rate in all directions, is the only suitable etching mechanism to form a spherical cavity and nearly perfect hemispherical shapes inside the wafer.

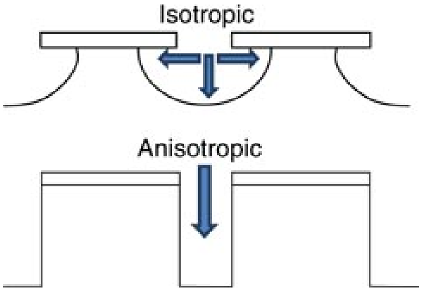

Figure 2.5: Anisotropic vs isotropic etching

For chemical wet etching, different well-known mixtures that are all based on nitric acid, HNO_3, can be used for this purpose. These include, for example, hydrofluoric-nitric mixture which is composed of 6 parts of HNO_3 (69%) with 1 part hydrofluoric acid, HF (49%), and 2 parts deionized water, DI (Svetovoy et al., 2006). Another common mixture that can be also used is the hydrofluoric acid-nitric acid-acetic acid, HNA, in the ratio (30:43:27) using acetic acid with concentration of 99.5% (Laliotis et al., 2012). The chemical reaction of these etching techniques is divided into two stages that started first by Si oxidation and followed by oxide removal. Nitric acid is a powerful oxidizing agent that offers the first stage of Si oxidation. The tough oxide film will be then etched by the hydrofluoric acid in the next phase of the reaction. Although these mixtures are commonly used, they are showing some dependency on Si crystal orientation. Moreover, for a trusted and consistent results, these solution should be used in a large volume and prepared long time before usage. The etching rate also changes dramatically with use as the solution becomes weaker (Williams et al., 2003).

Another wet etching technique also that can show isotropic etching profile for Si <100> is by using a well-known anisotropic potassium hydroxide, KOH, solution as reported by Kendall et al. (1994). Normally, etching in KOH forms a pyramidal cavity defined by the mask opening d_0 and limited to <111> planes as shown in Figure 2.6 (a) & (b). However, if the etching mask is removed and etching process has been kept running, the pyramidal cavity will be changed as shown in Figure 2.6 (c), (d) & (e). The continuation of the reaction is simply explained as follows: the edges between the <100> and <111> planes are attacked, exposing the fast etching <411> planes, which take over the <111> planes and render a new pyramidal pit with a new depth s as shown in Figure 2.6 (f). The tip of the pyramidal pit starts to be replaced by a smooth spherical shape while the <411> walls recede as shown in Figure 2.6 (g). The cavity top diameter D increases with further etching, while its depth remains unaltered as shown in Figure 2.6 (h) (Costa et al., 2009).

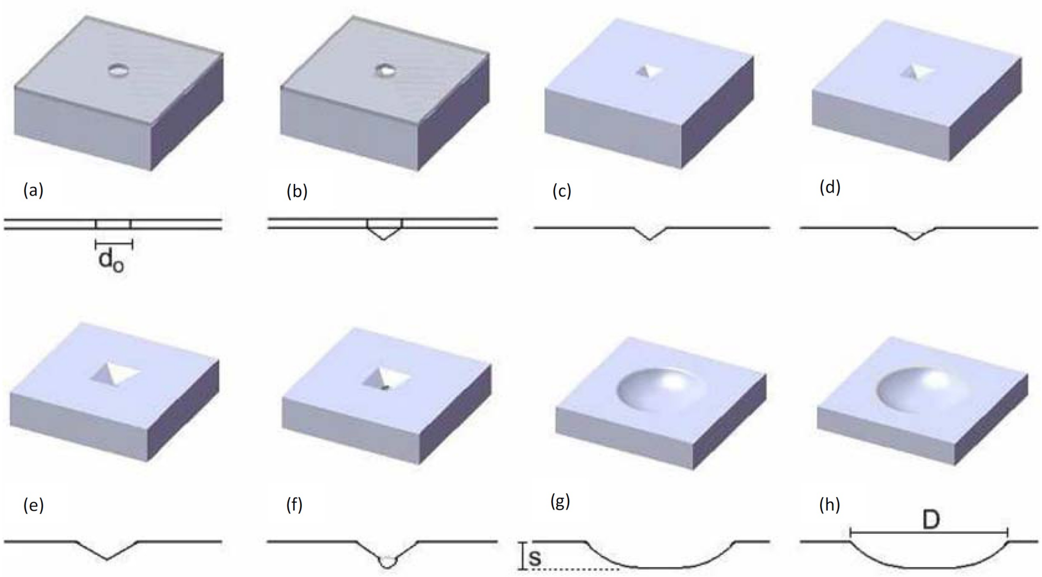

Figure 2.6: Isotropic etching of Si <100> in KOH

The standard isotropic xenon difluoride XeF_2 etching is another technique based on dry etching mechanism for silicon (Si) micro-machining which can be used to develop the complex three-dimensional micro-structures. In general, the XeF_2 etching has also a fast etching rate. The etching mechanism includes the primary chemical diffusion reaction which is given by:

$$2XeF_2 + Si \longrightarrow 2Xe \uparrow + SiF_4 \uparrow \tag{2.1}$$

It is therefore based on a gaseous phase chemical diffusion reaction of the fluorine ions into Si at room temperature to produce the volatile tetrafluorosilane (SiF_4) gas without any need of plasmas or catalysts Hajj-Hassan et al. (2010); Xuan et al. (2006). This will thus offer a very simple and cost effective solution while maintaining the CMOS compatibility. However, in addition to SiF_4, etch products have also been reported to include some trace amount of other different silicon fluoride byproducts, which make the reaction kinetics quite puzzling and yet not fully understandable Chan et al. (1999); Chu et al. (1997). Several authors had previously presented a detailed study and analysis of Si etching characteristics through this technique trying to give an estimate for the etching rate Chan et al. (1999); Chu et al. (1997); Su and Tabata (2002); Williams et al. (2003); Xuan et al. (2006). However, this technique shows a non-linear etching rate while being dramatically dependent on the loaded sample conditions as well as the pattern dimensions Chan et al. (1999); Chu et al. (1997); Su and Tabata (2002). Therefore, there is no prescription in the literature that can be generalized.

2.3 Antenna Design

The nano-antenna will provide irradiance harvesting and optimize energy transfer to the sub-wavelength localized sensor. Antenna performance (gain, directivity, resonance, impedance...etc.) will then greatly influence the detector characteristics. The antenna shape and geometry can be tailored for given requirements including, for example, resonant wavelength, spectral response, polarization, and angular response. Most of the challenges in the antenna design are encountered here mainly because of the air-dielectric interface. As a result, trapped surface waves will be always excited reducing the radiation efficiency of the antenna and causing crosstalk between neighboring antennas (Rutledge & Muha, 1982). Moreover, due to the new boundary conditions imposed on the electromagnetic fields through this interface, resonant wavelength, radiation pattern and antenna current distribution will be all changed compared to those placed in free space (Fumeaux et al., 1998). The electrical and optical properties of the materials will be also altered at the IR band representing another challenge in design. The finite effective electron mass in metals will result in delayed reaction to incident EM field as the frequency increases. The metals will not then behave as perfect conductors as before. Although plasmon resonance cutoff frequency is noticed sufficiently beyond the IR band, the conductivity of metals still drops considerably while skin depth increases at the LWIR band (Biagioni et al., 2012; Donchev et al., 2014). This will in turn result in attenuation, propagation losses and noise levels that will have impact on antenna current distribution and also antenna arrays whenever being of design interest. As a result, the surface impedance of the metal strip and Coleman effect, which may attribute also the antenna current distribution and cause attenuation, has to be considered and can not be neglected at this band although both were previously always excluded from calculations (Wilke, Herrmann, & Kneubühl, 1994).

Acquiring antenna design also with some dimensions that can fall in the range of tens of nanometers, the change of properties for nano-wire has to be also considered. In such cases, as the dimensions may become comparable to the electron mean free path, electron scattering will be increased, reducing in its turn thermal conductivity and thermoelectric properties of the metal (Russer et al., 2015; Szakmany et al., 2015). The heat distribution over the structure can then influence the antenna temperature and the performance as well when coupling to thermal sensor as bolometer or thermocouple.

2.3.1 Dielectric Half-Space and Angular Response

While the example of half wave dipole antenna shows symmetric angular response when operating in free space, this symmetry will be broken once the interface of two dielectrics exists as in the case of antenna coupled detectors. Thus, as shown in Figure 2.7, the antenna angular response will show higher sensitivity to radiation which is incident from the half space with the higher dielectric function, ε, (Fumeaux et al., 2000; Wilke, Herrmann, & Kneubühl, 1994) as follows:

$$\frac{P_{sub}}{P_{air}} = \left(\frac{\varepsilon_{sub}}{\varepsilon_{air}}\right)^{3/2} \tag{2.2}$$

where P_{sub}, ε_{sub}, P_{air}, ε_{air} are power and permittivity in both substrate and air respectively. The gain and directivity of the designed antenna will also follow the same